Commun. Comput. Phys.
doi: 10.4208/cicp.230410.090911s

Vol. **11**, No. 4, pp. 1182-1204
April 2012

High Efficient Numerical Simulation of Infrared Radiation from a Hot Exhaust Nozzle

Haiyang Hu[1], Peng Bai[1] and Qiang Wang[2,*]

[1] *China Academy of Aerospace Aerodynamics, Beijing 100074, P.R. China.*
[2] *School of Jet Propulsion, Beihang University, Beijing 100191, P.R. China.*

Received 23 April 2010; Accepted (in revised version) 9 September 2011

Communicated by Boo Cheong Khoo

Available online 29 November 2011

Abstract. A coupled model, capable of simulating transonic flow, solid heat conduction, species transport, and gas radiation, is developed that provides better computational treatment of infrared radiation from hot exhaust nozzles. The modeling of gas radiation is based on a statistical narrow-band correlated-k analysis, whose parameters are deduced from the HITEMP line-by-line database. To improve computational efficiency, several methods are employed. A mixed analytical-numerical algorithm is described for the stiffness of the two-equation turbulence model and an alternating direction implicit pretreatment for the ill-conditioned matrix appearing in the coupled problem of flow and solid heat conduction. Moreover, an improved multigrid method and a symmetry plane treatment of the radiation transfer-energy equations are also introduced. Four numerical simulations are given to confirm the efficiency and accuracy of the numerical method. Finally, an account of the aerothermodynamics and infrared characteristics for two types of nozzles are presented. The infrared radiation intensity of the Chevron ejecting nozzle is clearly smaller than that of the common axisymmetric ejecting nozzle. All computations can be performed on a personal computer.

AMS subject classifications: 65L20, 74A15, 76F60, 76H05, 78A40

Key words: Numerical simulation, infrared radiation, exhaust nozzle, stiffness of two-equation turbulence model.

1 Introduction

In recent years, infrared detection/stealth technology has developed rapidly. Some key techniques, such as the suppression of infrared radiation from exhaust systems crucial to stealth aircraft have attracted wide attention and keen investigation. The infrared

*Corresponding author. *Email addresses:* barbapapa@sjp.buaa.edu.cn (H. Hu), baipeng73@yahoo.com.cn (P. Bai), Qwang518@buaa.edu.cn (Q. Wang)

signature band of 3 to 5 μm from an aircraft's exhaust system corresponds to the infrared transmission window of air. As a consequence an aircraft's exhaust system becomes a primary target of heat-seeking missiles with infrared detectors.

There are several models to describe gas radiation characteristics. Among these, the line-by-line model [1] is accurate, but can only be used to validate other models. It is nearly impossible to use it to predict radiation from practical devices, because of its huge calculation overheads. The wide-band model [2] is often adopted to simulate gas radiation and heat transfer. The SNB (Statistical Narrow-Band) model [1], which generally involves 200-2 000 spectral bands, is often used to calculate gas infrared radiation intensity. The parameters of the SNB model are deduced from the HITEMP line-by-line database [3]. HITEMP is a database developed by Air Force Geophysics Laboratory [1] for high resolution atmosphere absorption lines.

However, a direct implementation of this model to radiation transfer in multi-dimensional geometries will encounter severe computational difficulties because it formulates the gas radiation behavior in terms of transmissivity (τ) rather than the more fundamental absorption coefficient (k). At present, this problem can be solved by the correlated-k model [4, 5]. Because the calculation still entails huge computational overheads with wide/narrow-band models, most researchers of these models calculate radiation intensities/heat transfers assuming that no correlation exists between radiation and other physical quantities [6].

In this paper, a coupled model is developed that can be used to calculate flow and solid heat conduction, gas radiation transfer and heat exchange, and species transport. To improve computational efficiency, several methods are employed, including a mixed analytical-numerical algorithm, an improved multigrid strategy, the Brian alternating direction implicit (BADI) pretreatment, and a symmetry-plane treatment of radiation. To confirm the efficiency and accuracy of our methods, four numeric calculations are presented, namely the pressure distribution around an axisymmetric nozzle, the temperature distribution of a rocket engine water-cooling nozzle, the radiation heat exchange within a cylindrical furnace, and the carbon dioxide radiation absorptivity at a wavelength of 4.3 μm. Finally, aero-thermodynamics and infrared characteristics of an axisymmetric ejecting nozzle (AEN) and a Chevron ejecting nozzle (CEN) are generated, which show that the algorithm has highly-improved computational efficiency.

2 Mathematical models

2.1 Coupled model between flow and solid heat conduction

The second-order Roe scheme [7] is employed to discretize the governing equations, which are the three-dimensional generalized Navier-Stokes equations [8]:

$$\frac{\partial}{\partial t}\iiint_V \mathbf{Q}\,dV+\oiint_S(\mathbf{F}-\mathbf{F}_V-\mathbf{F}_W)\,dS=\iiint_V \mathbf{G}\,dV, \tag{2.1}$$

where t is the pseudo time for the purpose of computing (used throughout all equations), $\mathbf{Q}=(\rho,\rho u,\rho v,\rho w,\rho e)^T$ the vector of primitive flow variables, ρ fluid density, $\mathbf{U}=u\mathbf{i}+v\mathbf{j}+w\mathbf{k}$ the velocity vector of flow field, e the fluid internal energy, $\mathbf{F}$ the convection flux vector of the flow field, $\mathbf{F}_V$ the diffuse flux vector of the flow field, $\mathbf{F}_w=(0\ 0\ 0\ 0\ \dot{q}_w+\dot{q}_{rw})^T$ the thermal flux of the solid wall, and $\mathbf{G}=(0\ 0\ 0\ 0\ \dot{q}_{rg})^T$ the gas radiative heat source.

Turbulence is modeled by the renormalized group (RNG) $k-\varepsilon$ (two-equations) model [9].

The conservation form of the three-dimensional solid-phase unsteady heat conduction equation is as follows:

$$\frac{\partial}{\partial t}\iiint_V \rho c T dV=\oiint_S \lambda\mathbf{n}\bullet\nabla T dS, \tag{2.2}$$

where c is the solid phase specific heat capacity, λ is the solid phase thermal conductivity, and $\mathbf{n}=n_x\mathbf{i}+n_y\mathbf{j}+n_z\mathbf{k}$ denotes the unit normal of the grid cell surface.

The third-type boundary condition (In numerical simulations of solid-phase heat conduction, the third-type boundary condition requires specifying the near wall fluid temperature and the convective heat transfer coefficient. See below for details.) is employed to deal with the coupling between flow field and the temperature field of the solid, because directly transferring the interface temperature and heat flux will cause computational instabilities, and even divergence [10, 11]. A typical one-dimensional model coupling flow and solid heat conduction is depicted in Fig. 1.

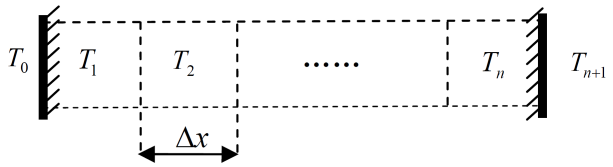

Figure 1: Schematic depiction of one-dimensional flow/solid heat transfer.

In Fig. 1, $T_1\sim T_n$ are unknown temperatures at sequential grid cells within the solid region. T_0 and T_{n+1} are the respective temperatures near the wall. If $\frac{\partial}{\partial t}=0$, a matrix form of the one-dimensional solid heat conduction equation taking into account convective heat transfer is as follows:

$$\begin{pmatrix} d_0+a & -a & & & \\ -a & 2a & -a & & \\ & & \ddots & & \\ & & -a & 2a & -a \\ & & & -a & d_{n+1}+a \end{pmatrix}\begin{pmatrix} T_1 \\ T_2 \\ \vdots \\ \vdots \\ T_n \end{pmatrix}=\begin{pmatrix} b_0 \\ 0 \\ \vdots \\ 0 \\ b_{n+1} \end{pmatrix}, \tag{2.3}$$

where $d=\frac{1}{1/h+\Delta x/2\lambda}$, $b_0=d_0T_0$, $b_{n+1}=d_{n+1}T_{n+1}$, $a=\frac{\lambda}{\Delta x}$, h is the convective heat transfer coefficient, and $\dot{q}_w=d_0(T_1-T_0)$.

2.2 Radiation transfer and energy equations

The conservation form of the radiation transfer equation is:

$$\int_{\Omega^m}\oiint_S I_\upsilon^m(\mathbf{s}^m\bullet\mathbf{n})dSd\Omega=\int_{\Omega^m}\iiint_V\left(\frac{k_\upsilon}{\pi}E_{b,\upsilon}-k_\upsilon I_\upsilon^m\right)dVd\Omega\Big|_{\forall\upsilon,m}, \tag{2.4}$$

where the unknown variable I_υ^m is the gas radiance at wave number υ and spatial angle Ω^m (with index m), $\mathbf{s}^m$ is the unit vector of Ω^m, k_υ is the gas absorption coefficient at wave number υ, $E_{b,\upsilon}=f(T,\upsilon)$ is the blackbody radiation emission energy at wave number υ, V and S are respectively the volume and surface area of the control domain, and $\mathbf{n}$ is the outward unit normal of S.

For the finite volume method (FVM) [1], the first-order discrete form of Eq. (2.4) is:

$$\begin{aligned}a_{w,i,j,k}I^m_{\upsilon,i-1,j,k}+a_{e,i,j,k}I^m_{\upsilon,i+1,j,k}+a_{s,i,j,k}I^m_{\upsilon,i,j-1,k}+a_{n,i,j,k}I^m_{\upsilon,i,j+1,k}\\ +a_{d,i,j,k}I^m_{\upsilon,i,j,k-1}+a_{u,i,j,k}I^m_{\upsilon,i,j,k+1}+a_{p,\upsilon,i,j,k}I^m_{\upsilon,i,j,k}=b^m_{\upsilon,i,j,k},\end{aligned} \tag{2.5}$$

where

$$\begin{aligned}a_{p,\upsilon,i,j,k}&=\sum_{x=w,e,s,n,d,u}\left(\int_{\Omega_m}\oiint_{S_x}\max(\mathbf{s}^m\bullet\mathbf{n},0)dSd\Omega+k_\upsilon V_{i,j,k}\Omega_m\right),\\ a_{x,i,j,k}&=-\int_{\Omega^m}\oiint_{S_x}\max(-\mathbf{s}^m\bullet\mathbf{n},0)dSd\Omega\Big|_{x=w,e,s,n,d,u},\\ b^m_{\upsilon,i,j,k}&=k_\upsilon\frac{E_{b,\upsilon}}{\pi}V_{i,j,k}\Omega_m,\end{aligned}$$

subscripts e, w, n, s, u, d denote grid cell surface positions relative to the grid center (p), and subscripts i, j, k are grid cell serial number. The boundary condition of the gas radiance for a diffuse reflective solid wall is:

$$I^m_{\upsilon,w}=\frac{\varepsilon_w E_{b,\upsilon}}{\pi}+\frac{1-\varepsilon_w}{\pi}\sum_{m,\mathbf{s}^m\bullet\mathbf{n}_w<0}^{4\pi}I_\upsilon^m\left|\mathbf{n}_w\bullet\mathbf{s}^m\right|d\Omega^m, \tag{2.6}$$

where subscript w identifies quantities associated with the solid wall, and ε_w is the solid-wall emissivity.

The radiation heat source of the gas and the radiation heat flux associated with the solid wall are obtained by solving the radiation energy equations [1] that are then incor-

porated into Eq. (2.1) as energy source terms. These are shown as follows:

$$\dot{q}_{rg}=\int_0^{+\infty}(-4k_\upsilon E_{b,\upsilon}+\sum_m^{4\pi}k_\upsilon I_\upsilon^m d\Omega^m)d\upsilon, \tag{2.7a}$$

$$\dot{q}_{rw}=\int_0^{+\infty}(-\varepsilon_w E_{b,\upsilon}+\varepsilon_w \sum_{m,\mathbf{s}^m\bullet\mathbf{n}_w<0}^{4\pi} I_\upsilon^m\left|\mathbf{n}_w\bullet\mathbf{s}^m\right|d\Omega^m)d\upsilon. \tag{2.7b}$$

2.3 Gas radiation model

Three parameters of the SNB model, namely the average gas absorption coefficient at the spectral band $\bar{k}_\upsilon(atm^{-1}\bullet cm^{-1})$ and the average interval $\bar{d}_\upsilon(cm^{-1})$ and average semi-width $\bar{b}_\upsilon(cm^{-1})$ of spectral lines, are deduced from the HITEMP line-by-line database [3,12]. The principle of the correlated-k model is that if a parameter ϕ_υ only depends on the gas absorption coefficients, then its integration over a wave band $\Delta\upsilon$ can be replaced by integration over the absorption coefficient k_υ. Finally, the following equation can be obtained [5]:

$$\frac{1}{\upsilon}\int_{\Delta\upsilon}\phi(k_\upsilon)d\upsilon=\int_0^1\phi(g^{-1})dg, \tag{2.8}$$

where $g(k_\upsilon)$ is a cumulative distribution function about k_υ, and is obtained through an inverse Laplace transformation [5] on the transmittance formula of the SNB model $(\tau(\bar{k}_\upsilon,\bar{d}_\upsilon,\bar{b}_\upsilon))$ [1]. Eq. (2.8) is evaluated using a four-point Gauss-Legendre integral [13]. The absorption coefficient of the gas mixture within the same band is the sum of the absorption coefficients of each species [5,14].

2.4 Gas species transfer equations

The conservation form of the gas species concentration equations is [15]:

$$\frac{\partial}{\partial t}\iiint_V\rho Y_i dV+\oiint_S(\rho Y_i\mathbf{U}\bullet\mathbf{n}+\mathbf{n}\bullet\mathbf{J}_i)dS=0\Big|_{i=1\sim3}, \tag{2.9a}$$

$$\mathbf{J}_i=-\left(\rho D_i\nabla Y_i+\frac{\mu_T}{Sc_T}\nabla Y_i\right)\Big|_{i=1\sim3}, \tag{2.9b}$$

where $Y_{0\sim3}$ are mass concentrations of N_2, O_2, H_2O (vapor), and CO_2, respectively, $D_{1\sim3}$ are species laminar diffusion coefficients, $Sc_T=0.7$, and μ_T the turbulent viscosity.

2.5 RNG K-ε turbulence model

The conservation form of transport equations for RNG $K-\varepsilon$ turbulence model is:

$$\frac{\partial}{\partial t}\iiint_V \rho K dV+\oiint_S(\rho UK-(\mu+\mu_T/\sigma_K)\mathbf{n}\bullet\nabla K)dS=\iiint_V(\mu_T S_{ij}-\rho\varepsilon)dV, \tag{2.10a}$$

$$\frac{\partial}{\partial t}\iiint_V \rho\varepsilon dV+\oiint_S(\rho U\varepsilon-(\mu+\mu_T/\sigma_K)\mathbf{n}\bullet\nabla\varepsilon)dS=\iiint_V(\frac{C_{1\varepsilon}^*\varepsilon}{K}\mu_T S_{ij}-C_{2\varepsilon}\rho\frac{\varepsilon^2}{K})dV, \tag{2.10b}$$

where K is the turbulent kinetic energy, ε the turbulent kinetic energy dissipation rate, $U=\mathbf{U}\bullet\mathbf{n}$, μ the gas laminar dynamic viscosity, $\mu_T=C_\mu\rho K^2/\varepsilon$ the gas turbulent viscosity, $C_{1\varepsilon}^*=C_{1\varepsilon}-\frac{\eta(1-\eta/\eta_0)}{1+\beta\eta^3}$, $\eta=\sqrt{2S_{ij}S_{ij}}\frac{K}{\varepsilon}$, $S_{ij}=\frac{1}{2}(\frac{\partial u_i}{\partial x_j}+\frac{\partial u_j}{\partial x_j})$, and C_μ, $C_{1\varepsilon}$, $C_{2\varepsilon}$, β, η_0, σ_K are model constants.

3 The Methods to improve computational efficiency

The discrete forms for the three-dimensional solid-phase heat conduction and radiation transfer equations (Eq. (2.2) and (2.4) resp.) are similar (see Eq. (2.5)); when the orthogonality of the grid used in solving Eq. (2.2) is adequate and the spatial-angle resolution for solving Eq. (2.4) is high enough $(d\Omega_m\to 0)$, the coefficient matrices of their discrete form will be diagonally dominant. Thus the same algorithm is used to solve both. In this case, this results in high computational efficiency, low memory cost, and favorable computational stability, when the BI-CGSTAB (bi-conjugate gradient stabilized) [16] algorithm with the precondition matrix is used to solve Eqs. (2.2) and (2.4).

The steady-state forms of the N-S equation Eq. (2.1), species transport equations (2.9), and turbulence model transport equations (2.10) are either hyperbolic or parabolic partial differential equations. The coefficient matrices of their discrete form is not diagonally dominant. To ensure computational stability, the pseudo time "t" is added and the time marching algorithm is used to solving these. The LUSGS [17] (lower upper symmetric Gauss-Seidel) implicit time-marching method with multigrid acceleration is employed to solve Eq. (2.1). The $K-\varepsilon$ equations are only solved on the fine grid because the gradient of ε and its source term in the near-wall region is too large and the coarse grid correction algorithm would encounter difficulties guaranteeing computational stability. The species transport equations are only solved on the coarse grid because its accuracy on the coarse grid is good enough to meet requirements of computational accuracy; solving on the fine grid would evoke a greater computational burden.

3.1 The mixed analytical-numerical algorithm

In regard to jet flows, a numerical test has indicated that the primary factor affecting computational efficiency is the stiffness arising in the two-equation turbulence model. [18]

points out that for explicit time-marching methods, high aspect ratio meshes are primarily cause of stiffness in the two-equation turbulence model. For conventional explicit time-marching methods,

$$\Delta t=\frac{CFL\bullet\Delta x\Delta y}{(|u|+c)\Delta y+(|v|+c)\Delta x},$$

where x is the direction parallel to the solid wall surface. The grid spacing in the x-direction is Δx, while the boundary layer flow velocity component in the x-direction is u; y is the direction perpendicular to solid wall surface with grid spacing of Δy, and the flow velocity component in the y-direction is v. c is the velocity of sound, and $u+c$ and $v+c$ are of the same order. With $CFL\leq 1$, the tolerance for Δt in each iteration is much smaller than the N-S equations iteration time step. Thus this will generate "stiffness".

Neglecting the diffusion term and the gas density change, Eq. (2.10) can be written as:

$$\frac{\partial\mathbf{W}}{\partial t}+\Lambda\frac{\partial\mathbf{W}}{\partial x}=\mathbf{G}(\mathbf{W}),\qquad \Lambda=\begin{bmatrix}\lambda_T & \\ & \lambda_T\end{bmatrix}=\begin{bmatrix}U & \\ & U\end{bmatrix},\tag{3.1}$$

where $\mathbf{W}=(K,\varepsilon)^T$. Because the source item

$$\mathbf{G}(\mathbf{W})=\left(C_\mu\frac{K^2}{\varepsilon}S_{ij}-\varepsilon,\ C_{1\varepsilon}^*C_\mu KS_{ij}-C_{2\varepsilon}\frac{\varepsilon^2}{K}\right)^T$$

is well-posed, if Harten's flux modification second-order explicit scheme [19] is employed, Eq. (3.1) satisfies the total variation diminishing (TVD) property for $\lambda_T\frac{\Delta t}{\Delta x}\leq 1$. Thus Δt is obtained by:

$$\Delta t=\frac{CFL\bullet\Delta x\Delta y}{|u|\Delta y+|v|\Delta x}.\tag{3.2}$$

For boundary-layer flows, the normal component of the wall velocity is far smaller than the tangential component, *i.e.*, $v/u\ll 1$, hence Eq. (3.2) just offsets the disadvantage caused by $\Delta x/\Delta y\gg 1$ and therefore overcomes the above-mentioned stiffness. The second-order Runge-Kutta method may be omitted here on account of the algorithm's strict TVD property (being different to using the TVD scheme to solve N-S equations, its TVD property no long holds when Eq. (2.1) is re-expressed in the form of Eq. (3.1) by left multiplication of a characteristic matrix [19]), and the diminishing of the total variation is a sufficient condition indicating iteration convergence. This can increase computational efficiency by a factor of 2.

In accounting for the diffusion term, Eq. (3.2) is revised as:

$$\Delta t=CFL\frac{\Delta x\Delta y}{\left(|u|+\frac{2(\mu+\mu_T/\sigma_K)}{\rho\Delta x}\right)\Delta y+\left(|v|+\frac{2(\mu+\mu_t/\sigma_K)}{\rho\Delta y}\right)\Delta x}.\tag{3.3}$$

Meanwhile, we must pay attention to the fact that the above analysis is based on the foundation that the N-S equations and the turbulence transport equation are solved separately. Numerical simulations indicate that the above method does not satisfy the TVD property for a coupled iteration.

If the implicit algorithm is employed with a larger iteration time step, the source term of the turbulence transport equation will become the primary factor causing computation stiffness. The reason is that in the near-wall region when velocity gradients are great or in the region where model parameters diverge rapidly, the time-scale associated with the source term is far smaller than that of the convection-diffusion term for implicit iteration. The mixed analytical-numerical algorithm in the literature [20,21] can be used as a reference method.

First, one solves the convection-diffusion term:

$$\iiint_V \frac{\partial w}{\partial t} dV + \oiint_S F(w) - F_V(w) dS = 0 \Big|_{w(t^n)=w^n}^{t^n<t<t^{n+1}}, \tag{3.4}$$

and w^* is obtained. Here w is K or ε, $F(w)$ is UK or $U\varepsilon$, $F_V(w)$ is $(\mu+\mu_T/\sigma_K)\mathbf{n}\bullet\nabla K/\rho$ or $(\mu+\mu_T/\sigma_K)\mathbf{n}\bullet\nabla\varepsilon/\rho$, $G(w)$ is $C_\mu\frac{K^2}{\varepsilon}S_{ij}-\varepsilon$ or $C^*_{1\epsilon}C_\mu KS_{ij}-C_{2\varepsilon}\frac{\varepsilon^2}{K}$; superscript n denotes iteration step (used throughout all equations).

Second, one then solves the source term:

$$\frac{\partial w}{\partial t} = G(w) \Big|_{w(t^n)=w^*}^{t^n<t<t^{n+1}}, \tag{3.5}$$

and w^{n+1} is obtained. Eq. (3.5) is analytically integrable [21].

An explicit iteration with a small time marching step is still used in [20] to solve the turbulence transport equations. The reason lies in nonlinearity of the convection-diffusion term and the turbulence source term, which cause bad convergence within the above algorithm when a larger iteration time step is used, namely

$$\iiint_V G(w) dV - \oiint_S F(w) - F_V(w) dS = 0 \Rightarrow w^{n+1} - w^n \neq 0. \tag{3.6}$$

The improved mixed analytical-numerical algorithm used here is as follows:

$$G^* = G(w^*), \qquad w^* = w^n + \int_{t^n}^{t^{n+1}} \left(G(w) - \frac{1}{V} \oiint_S F^n - F_V^n dS \right) dt \tag{3.7}$$

$$(w^{n+1}-w^n)\left(\frac{V}{t^{n+1}-t^n} + \oiint_S \frac{\partial F - F_V}{\partial w} dS \right) + \oiint_S F^n(w) - F_V^n(w) dS = \iiint_V G^* dV, \tag{3.8}$$

where Harten's flux modification second-order TVD scheme, mentioned above, is employed to discretize the convection-diffusion term, so that the algorithm is convergent. Regarding the standard $K-\varepsilon$ model, Eq. (3.7) can be solved through the analysis method referred to in the literature [21]. For various improved $K-\varepsilon$ models, such as the RNG

$K-\varepsilon$ model and several low Re number $K-\varepsilon$ models, Eq. (3.7) can be simplified to the standard $K-\varepsilon$ models through freezing certain variables or using an explicit single-step process to calculate integrals approximately. The maximum integration time step interval (dt) should be used to guarantee that integral errors are controllable [22,23]; that is:

$$\frac{1}{dt}>\max\left(\left|\frac{G(K,\varepsilon)}{K}\right|,\left|\frac{G(K,\varepsilon)}{\varepsilon}\right|,\frac{\varepsilon}{(2-C_{2\varepsilon})K}\right). \tag{3.9}$$

For Eq. (3.8), the maximum time marching step is adopted to guarantee that the implicit time marching method cannot obtain negative w values [22,23]; that is:

$$\frac{1}{\Delta t}=\frac{1}{t^{n+1}-t^n}>\frac{\left|G(w)-\frac{1}{V}\oiint_S F^n-F_V^n dS\right|}{w}. \tag{3.10}$$

3.2 An improved multigrid strategy

In regard to implicit iteration, the efficiency of the multigrid strategy is not so effective as in the explicit iteration. All examples in this paper only adopt a double-grid technique. The coarse grid is obtained by merging eight neighboring fine grids. The V cycle in the coarse grid correction FAS scheme is employed. Every 15 iterative steps on the fine grid is followed by 35 iterative steps on the coarse grid. To overcome solution oscillations caused by coarse grid corrections when a high aspect ratio grid is adopted [23], we make the following improvement: the correction value in the fine grid ($\Delta\mathbf{Q}_f$), obtained through trilinear interpolation of the coarse grid correction value ($\Delta\mathbf{Q}_c$), is not added to the fine grids directly. A new alternative is:

$$(\mathbf{Q}^{n+1}-\mathbf{Q}^n)\left(\frac{V}{\Delta t}+\oiint_S\frac{\partial\mathbf{F}-\mathbf{F}_V}{\partial Q}dS\right)=-\oiint_S\mathbf{F}^n-\mathbf{F}_V^n dS+\frac{V}{\Delta t}\Delta\mathbf{Q}_f. \tag{3.11}$$

It can be seen that, if an explicit iteration is adopted for the fine grid, the above process will change to

$$(\mathbf{Q}^{n+1}-\mathbf{Q}^n)\frac{V}{\Delta t}=-\oiint_S\mathbf{F}^n-\mathbf{F}_V^n dS+\frac{V}{\Delta t}\Delta\mathbf{Q}_f. \tag{3.12}$$

This is the same as adding $\Delta\mathbf{Q}_f$ to the fine grid directly. For the implicit algorithm of Eq. (3.11), the above process is equal to smoothing $\Delta\mathbf{Q}_f$.

3.3 The BADI pretreatment

When the solid region is quite thin and the heat conduction coefficient is large, a in Eq. (2.3) will be much higher than h, and thereby $\varepsilon\approx h\ll a$. For example, for the near-wall grid, $y^+\approx 30$ is used to obtain good accuracy [15], and ε/a is about 0.001. If the

matrix forms of Eqs. (2.2) and (2.3) are written as:

$$\mathbf{A}_{3-D}\mathbf{T}=\mathbf{B}, \qquad \mathbf{A}_{1-D}\mathbf{T}=\mathbf{B}, \tag{3.13}$$

then A_{1-D} is a typical ill-conditioned matrix with a high condition number [15].

To get high efficiency and stability for the BI-CGSTAB algorithm, pretreatment of matrix **A** must be adopted to lower its condition number. There are two kinds of pretreatments called left and right pretreatments:

$$\mathbf{M}_L^{-1}\mathbf{A}\mathbf{T}=\mathbf{M}_L^{-1}\mathbf{B} \quad \Leftrightarrow \quad \mathbf{A}'\mathbf{T}=\mathbf{B}', \tag{3.14a}$$

$$\mathbf{A}\mathbf{M}_R^{-1}\mathbf{M}_R\mathbf{T}=\mathbf{B} \quad \Leftrightarrow \quad \mathbf{A}'\mathbf{T}'=\mathbf{B}. \tag{3.14b}$$

Pretreated matrices must satisfy two requirements: first, these must be similar to matrix **A**; second, equation $\mathbf{M}\mathbf{X}'=\mathbf{X}$ must be easily solved. The commonly used pretreated matrices are LUSGS and ILU(0) [24], which are based on the approximate LU factorization of matrices. Actually, the effects by different matrices and different pretreatment have no obvious difference, and they are unable to effectively reduce the condition numbers of $\mathbf{A}_{1-D}$ and $\mathbf{A}_{3-D}$.

Compared with a much earlier Peaceman-Rachford alternating direction implicit algorithm, the advantage of the BADI algorithm for numerical heat transfer is to allow unrestricted iterative time steps [25]. When $\Delta t\to\infty$, the matrix form of a complete iterative step to solve Eq. (2.2) using the BADI algorithm is:

$$\mathbf{U}=(\mathbf{D}+\mathbf{X})^{-1}(\mathbf{B}-\mathbf{Y}\mathbf{T}^n-\mathbf{Z}\mathbf{T}^n), \tag{3.15a}$$

$$\mathbf{V}=(\mathbf{D}+\mathbf{Y})^{-1}(\mathbf{B}-\mathbf{X}\mathbf{U}-\mathbf{Z}\mathbf{T}^n), \tag{3.15b}$$

$$\mathbf{T}^{n+1}=(\mathbf{D}+\mathbf{Z})^{-1}(\mathbf{B}-\mathbf{X}\mathbf{U}-\mathbf{Y}\mathbf{V}), \tag{3.15c}$$

where the matrix coefficients **X**, **Y**, and **Z** consist of the pairs $a_{w,i,j,k}$ and $a_{e,i,j,k}$, $a_{s,i,j,k}$ and $a_{n,i,j,k}$, and $a_{d,i,j,k}$ and $a_{u,i,j,k}$, respectively. The diagonal matrix **D** has entries $a_{p,i,j,k}$. With $\mathbf{A}_{3-D}=\mathbf{D}+\mathbf{X}+\mathbf{Y}+\mathbf{Z}$, Eq. (3.15) can be rewritten as:

$$\mathbf{T}^{n+1}=\mathbf{T}^n+(\mathbf{D}+\mathbf{Z})^{-1}\mathbf{D}(\mathbf{D}+\mathbf{Y})^{-1}\mathbf{D}(\mathbf{D}+\mathbf{X})^{-1}(\mathbf{B}-\mathbf{A}_{3-D}\mathbf{T}^n), \tag{3.16}$$

and $\mathbf{M}_{BADI}=(\mathbf{D}+\mathbf{Z})^{-1}\mathbf{D}(\mathbf{D}+\mathbf{Y})^{-1}\mathbf{D}(\mathbf{D}+\mathbf{X})^{-1}$ is the left pretreated matrix used here. $(\mathbf{D}+\mathbf{X})^{-1}$, $(\mathbf{D}+\mathbf{Y})^{-1}$, and $(\mathbf{D}+\mathbf{Z})^{-1}$ are tridiagonal. The product of a tridiagonal matrix and vector is solved by the chasing method [13].

The pretreated matrix can reduce the condition numbers of $\mathbf{A}_{1-D}$ and $\mathbf{A}_{3-D}$ quite effectively. For example, when $n=5$ and $d=0.001a$, $cond(\mathbf{A}_{1-D})_\infty=10\,008.0\approx 10a/d$, $cond(\mathbf{M}_{LUSGS}^{-1}\mathbf{A}_{1-D})_\infty=5\,008.5\approx 5a/d$, and $cond(\mathbf{M}_{BADI}^{-1}\mathbf{A}_{1-D})_\infty=cond(\mathbf{E})_\infty=1$.

3.4 The treatment of symmetry plane for radiation transfer equation

The computation here treats the radiation transfer symmetry plane as a mirror surface (following the mirror-reflection law). The symmetry plane and the non-blackbody (diffuse reflection) solid wall provide boundary conditions used in solving Eq. (2.4). Their

incident radiances from certain spatial angles Ω^m are obtained from iterations. See Section 4.3 for an outline of the principle behind the radiation symmetry plane and a related numerical simulation example.

This technique does not decrease the CPU time if used in solving only the radiative transfer equations because computing mirror reflections actually increase iteration times, but it does reduce memory usage dramatically. However, if the treatment is used to solve the radiation field coupled with other physical fields, the CPU time and memory usage will decrease remarkably.

4 Validations

Four calculations are used to confirm the effectiveness of the above methods, each involving the supersonic flow, coupling between flow and solid heat conduction, radiation transfer, and radiation heat exchange. The program was compiled on an ICC 9.1 and operated on Intel Core2Duo E8400 CPU (master frequency is 3.0 GHz). The computation only uses one core of CPU.

4.1 Axisymmetric convergent-divergent nozzle

The axisymmetric convergent-divergent nozzle (AN) has a throat with a diameter of 128.63 mm. The largest external diameter of the nozzle is 152.4 mm, and the contraction and expansion angles for the outer and inner walls are 15.05° and 2.12°, respectively [26]. The computational boundary conditions involve the following settings: NPR (nozzle pressure ratio) was 10.1 and the ambient air velocity was Ma=1.2.

Block-structured grids were used in this and throughout all computations; the total grid cell number was about 870 000, the largest grid aspect ratio being nearly 100.

The computational grids, predicted Mach number contours, and turbulent kinetic energy distribution of the nozzle's inner-outer flow are shown in Fig. 2. The outer flow field creates an obvious boundary layer separation induced by the shock wave.

Computational residual convergence histories for different algorithms are shown in Fig. 3, where I denotes the mixed analytical-numerical (implicit) algorithm, E denotes the flux modification explicit scheme, and T denotes traditional method each of which were used in solving the turbulence model equation; in the determination of the N-S solution, M denotes that the multigrid strategy mentioned above was employed while S denotes that only a single grid was employed; "residual" is in reference to the N-S equation iteration residual, "residualK" is in reference to the $K-\varepsilon$ model equations iteration residual (used throughout all computations).

It can be seen that, when using the implicit algorithm with multigrid acceleration to solve the N-S equations, the stiffness of the two-equation turbulence model resulted in a calculational bottleneck. The mixed analytical/implicit-iteration algorithm can be clearly seen to enhance the calculation efficiency compared with other algorithms. Comparison

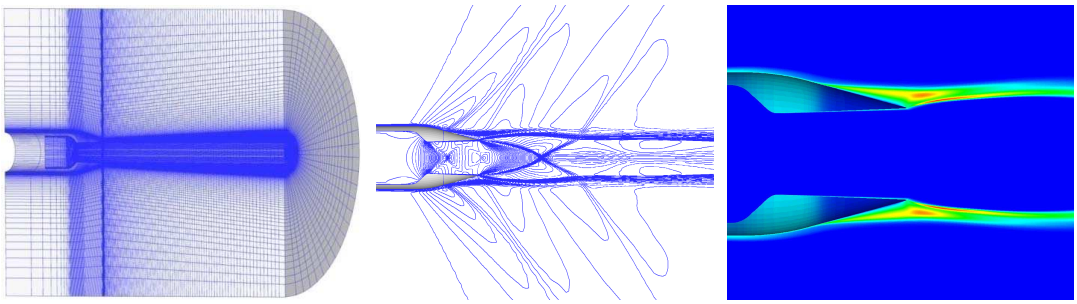

Figure 2: Computational grids, Mach number contours, and turbulent kinetic energy distribution.

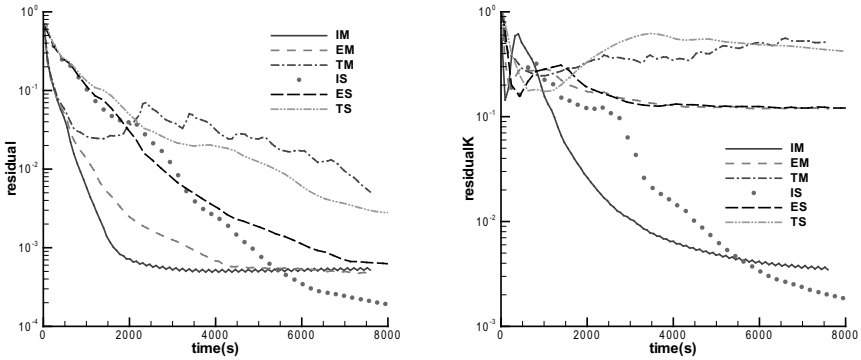

Figure 3: Computation convergence history of axisymmetric nozzle flow field.

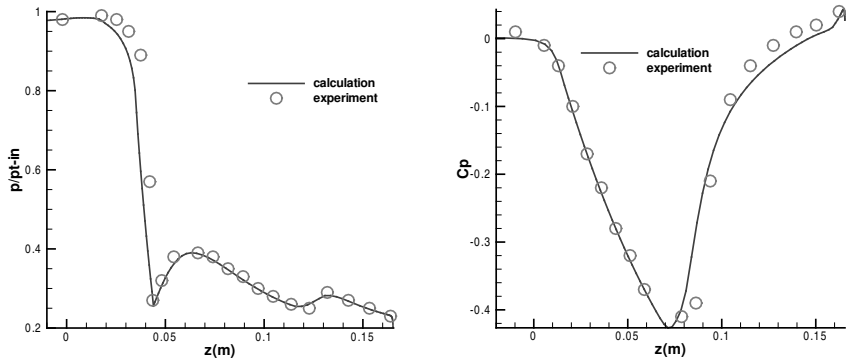

Figure 4: Inner (left) and outer (right) wall surface pressure distributions of an axisymmetric nozzle.

of computed results and experiment data [26] for the inner-outer wall surface pressures of the nozzle is shown in Fig. 4.

4.2 Water-cooling nozzle in rocket engines

As shown in Fig. 5, an axisymmetric nozzle was elected in demonstrating water cooling within a rocket engine [27]. The NPR was set at 5.1, and the inlet total temperature was

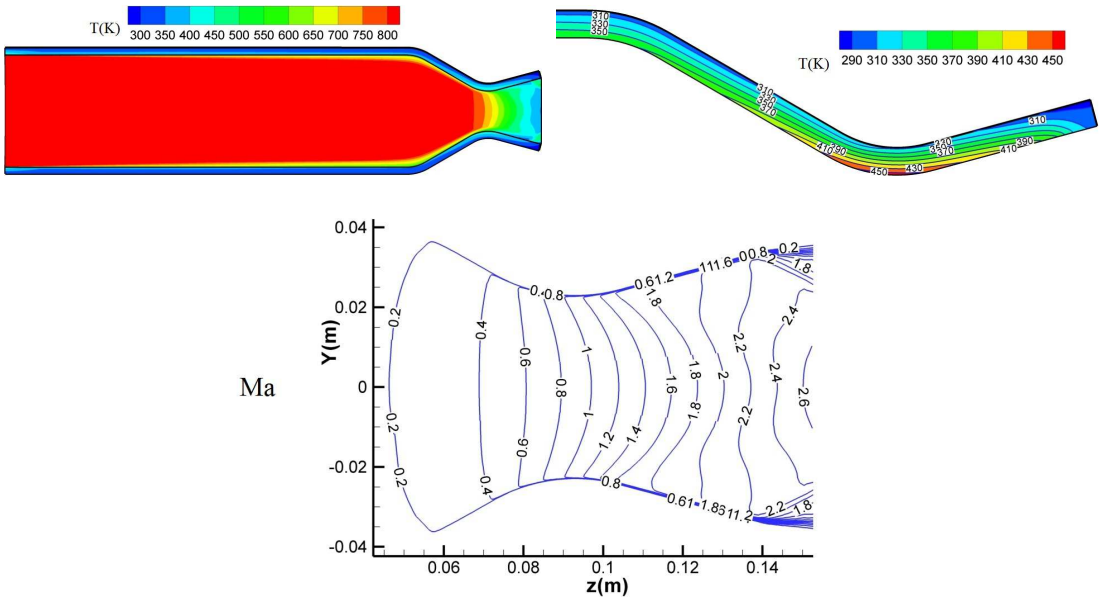

Figure 5: Mach number and temperature distribution of the water-cooled nozzle.

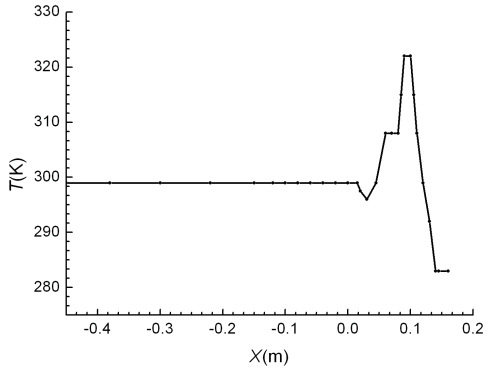

Figure 6: Temperature distribution of the nozzle outer wall[27].

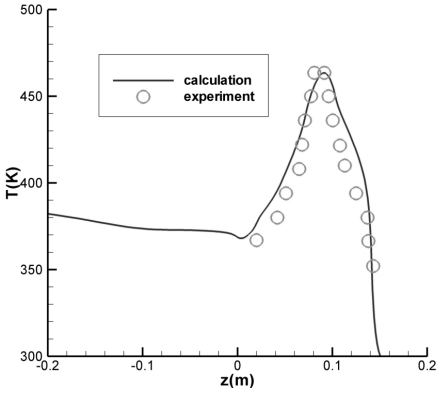

Figure 7: Temperature distribution of the nozzle inner wall.

843.33 K. The outer wall temperature distribution was given by test, as shown in Fig. 6. Simulation of the temperature distribution of the inner wall of the nozzle agreed well with experimental results (see Fig. 7).

4.3 Cylindrical furnace

The furnace is a hypothetic cylinder chamber 6m in length and 2 m in diameter. The furnace wall is assumed to be a black-surface at a temperature of 500 K. The temperature distribution of the gray gas in the furnace [28] is shown in Fig. 8.

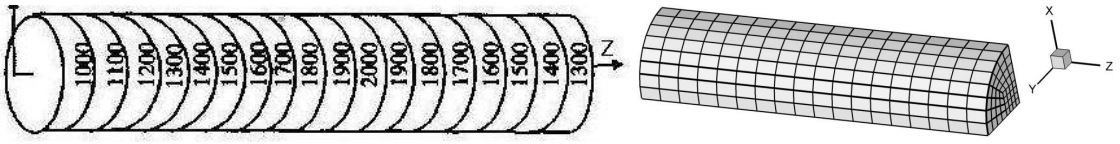

Figure 8: Temperature distribution of gas and computation grids.

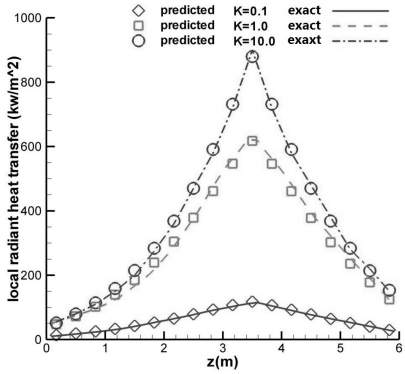

Figure 9: Comparison of predicted results and exact solutions[28] of furnace wall radiation heat transfer.

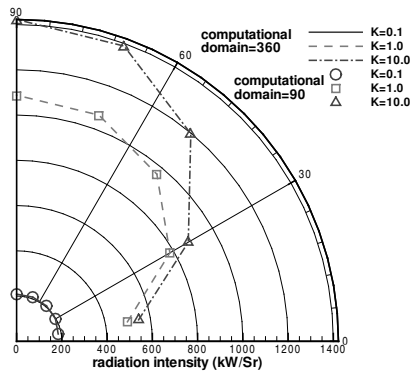

Figure 10: Comparison of gas radiation intensity distributions for different computational domains.

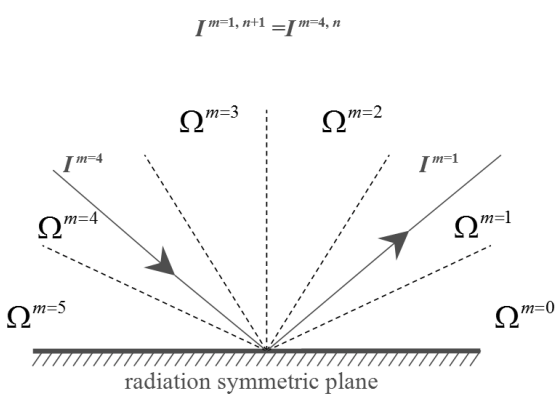

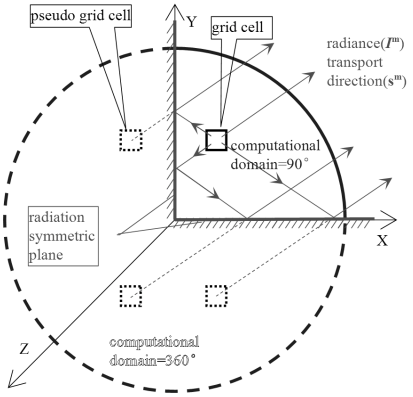

Figure 11: Sketch of the principle underlying the radiation symmetric plane.

The computational grids were coarse in this case, and the resolution of spatial angle reached only 10×10 (angle of circumference by zenith angle, same as below), although the simulation of the wall radiation heat flux agreed satisfactorily-well with exact solutions [28] (Fig. 9).

The distribution of gas radiation intensities for different detection directions (angle with z axis) under the assumption of a completely-transparent furnace wall are shown in Fig. 10. It can be seen that the results obtained in the quadrant computational domain (using two radiation symmetric planes simultaneously, the sketch is shown in Fig. 11)

agree very well with that in the complete computational domain, thus implying that the method described in Section 3.4 is very effective.

4.4 Gas spectral absorptivity

The database of the SNB model parameters for each spectral band was deduced with the method described in Section 2.3. Partial results for H_2O (vapor) at 2.7 microns are listed in Table 1; these are completely consistent with published literature [29].

Table 1: SNB model parameters for H_2O (vapor) at 2.7 microns

	500 K			1 000 K		
$\upsilon(cm^{-1})$	$k_\upsilon(atm^{-1}\bullet cm^{-1})$	$1/d_\upsilon(cm^{-1})$	$b_\upsilon(cm^{-1})$	$k_\upsilon(atm^{-1}\bullet cm^{-1})$	$1/d_\upsilon(cm^{-1})$	$b_\upsilon(cm^{-1})$
3300	0.0106	2.3295	0.0344	0.0546	7.9797	0.0215
3350	0.0187	2.4099	0.0358	0.0948	6.6236	0.0223
3400	0.0347	2.2523	0.0361	0.1490	6.0435	0.0226
3450	0.0599	1.9840	0.0360	0.2097	4.5005	0.0225
3500	0.1898	1.8879	0.0366	0.3684	4.3366	0.0229
3550	0.3185	1.7585	0.0379	0.3528	4.4485	0.0237
3600	0.4796	1.2362	0.0363	0.3383	3.9308	0.0227
3650	0.3850	1.1915	0.0363	0.3007	4.7914	0.0227
3700	0.6716	1.9464	0.0362	0.5272	3.9029	0.0227
3750	0.2119	1.4564	0.0346	0.1237	5.5833	0.0217
3800	0.3862	1.1784	0.0341	0.1843	4.6281	0.0213
3850	0.6092	1.4209	0.0320	0.3769	3.7005	0.0200
3900	0.3524	1.3582	0.0295	0.3889	3.1646	0.0185
3950	0.0752	1.6109	0.0278	0.1979	3.2424	0.0174

Comparison of the CO_2 absorptivities at wavelength of 4.3 microns predicted by SNB, the FVM-SNB correlated-k (CK) models, and Ludwig experiment data [30] are shown in Fig. 12. Calculation conditions were as follows: P=15 900 Pa, T=1 200 K, thickness L=15.05

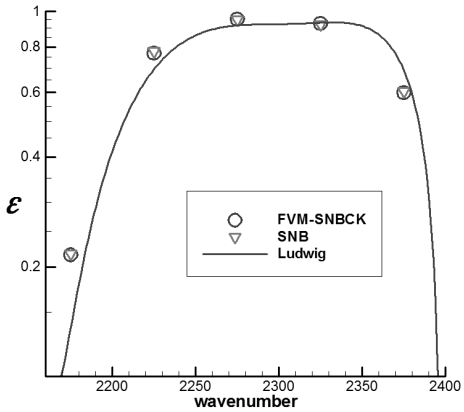

Figure 12: Comparison of CO_2 absorptivities at 4.3 microns from modeling and experiment [30].

cm, and CO_2 concentration of 100%. The 1-D computational grid number used in the finite-volume method was 10.

5 Applications

5.1 Axisymmetric ejecting nozzle (AEN)

The axisymmetric ejecting nozzle is composed of a primary nozzle and an ejecting sleeve. The primary nozzle is the same as described in Section 4.1. The height of the annular ejecting passage between the primary nozzle and the sleeve is 9.0 mm, and the thickness of the wall of the sleeve is 1.0 mm.

The computational domain covered a quadrant about the axial direction, and the total grid number was about 830 000, as shown in Fig. 13; there red grids denote the stainless steel primary nozzle, green grids denote the sleeve structure composed of aluminium alloy, and blue grids denote the flow field (the same color scheme is used throughout).

The boundary conditions were given as follows: the primary nozzle inlet total pressure was 511 691 Pa, total temperature was 1 500 K, H_2O (vapor) and CO_2 in the gas were generated from the chemical reaction of inner air (only 67% of air in primary nozzle participated in the reaction) and fuel (C_8H_{16}). The ambient air velocity was Ma=0.6 near the ground. The inlet air total pressure in the annular ejecting passage was set at 99% of the ambient total pressure, and the total temperature was equal to ambient total temperature. The solid surface radiation emissivity of 0.8 (by oxidation) corresponds to that of the metal of the nozzle.

Every 60 multigrid V iterations of the flow field, solid temperature and gas species concentration would be followed with an iteration of the radiation transfer equation, which was solved over just the coarsest grids (8 adjacent coarse grids merged together). The resolution of the spatial angle was 8×9. Next, $\dot{q}_{rg}$ and $\dot{q}_{rw}$, obtained by solving radiation energy equations on the coarsest grids, would be incorporated into the fine grids through trilinear interpolation.

The gas radiative heat source distribution of near wall boundary layer is shown in Fig. 14. Higher temperatures were obtained for gas closest to the wall; in consequence, more energy will radiate to the surrounding low temperature gas/wall. With both gas and solid radiation, the predicted wall temperature was higher than with solely solid radiation (Fig. 15). The reason is that the gas in the primary nozzle is at a higher temperature than solid wall.

5.2 Chevron ejecting nozzle (CEN)

Eight Chevron trailing edges were attached to the primary nozzle of the axisymmetric ejecting nozzle around the circumference. All other geometric parameters, grid-topology, y^+ of near wall grid cells and computational boundary conditions were kept the same as

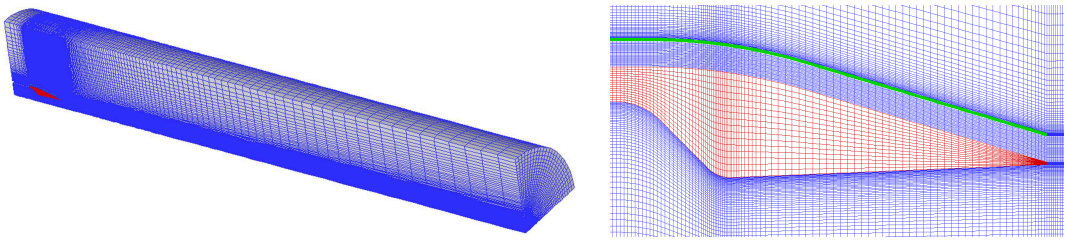

Figure 13: Computational grids for the axisymmetric ejecting nozzle.

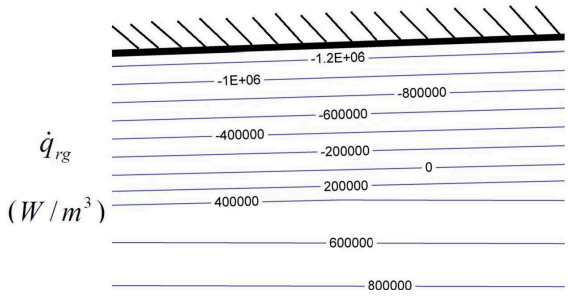

Figure 14: Gas radiative heat source distribution in the boundary layer of nozzle inner wall.

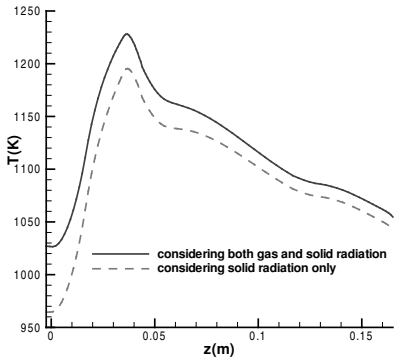

Figure 15: Predicted temperature distribution of nozzle inner wall.

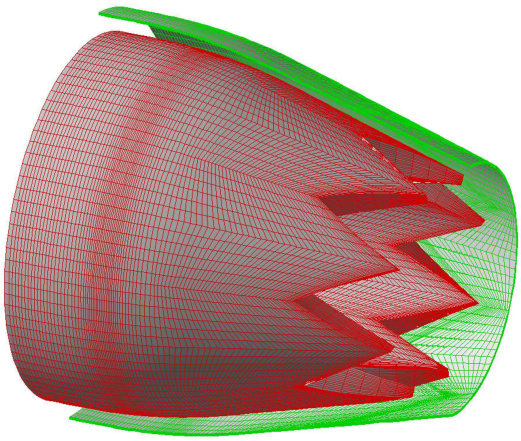

Figure 16: Computational grids for the Chevron ejecting nozzle.

those in Section 5.1. The total grid number was increased to about 890 000, as depicted in Fig. 16.

The residual convergence history and occupying CPU time ratio of the above two applications are shown in Fig. 17 and Table 2. Memory usage for the whole computation was 1.6 GB. Almost two-thirds of the whole computing time was spent in solving the gas

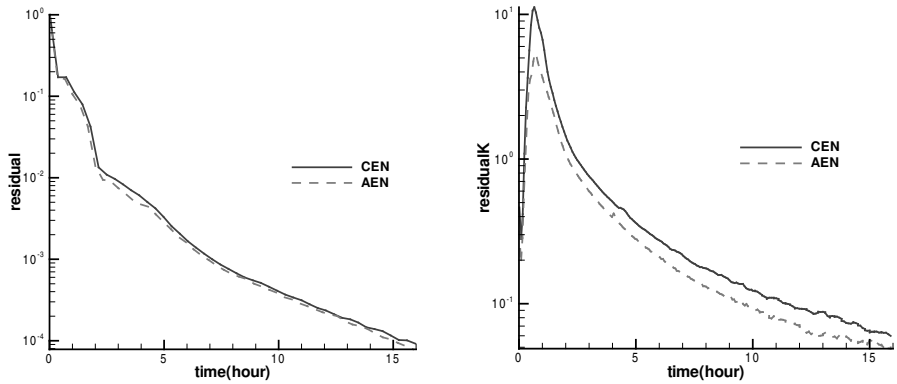

Figure 17: Computation convergence history of the two applications.

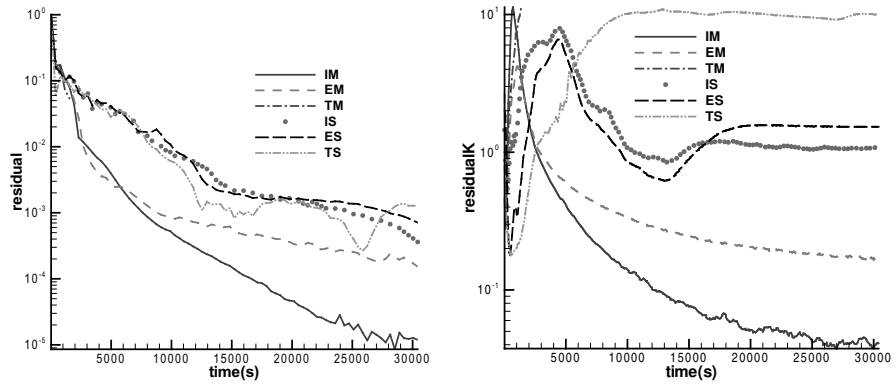

Figure 18: Computation convergence history of the Chevron ejecting nozzle.

radiation transfer equations. For just the solid radiation of the CEN, computational residual convergence histories of different algorithms are shown in Fig. 18. Compared with Section 4.1, the stiffness of the two-equation turbulence model had a greater influence on the convergence speed of the flow field, solid temperature field, species concentration field, and radiation heat transfer coupling computation. For the TM scheme, the larger coupling stiffness caused the computation divergence due essentially to the great disparity in iteration time steps between the N-S equations and the turbulence model equations.

Table 2: CPU time of each term.

Computational term	CPU time (%)
Flow field	31.8
Solid temperature	1.3
Species concentration	1.6
Radiation transfer and energy	65.3

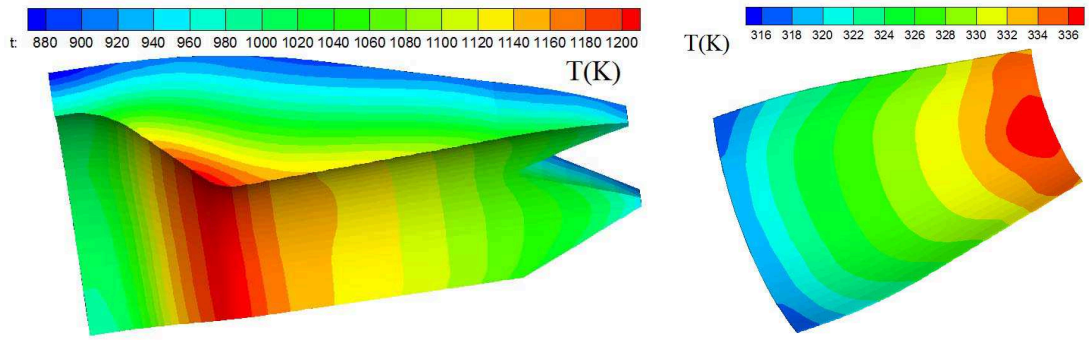

Figure 19: Temperature distributions of the primary nozzle (left) and the sleeve (right).

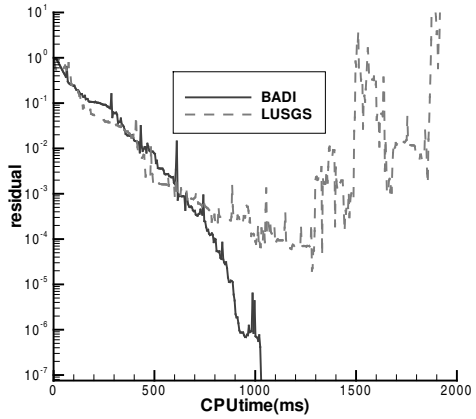

Figure 20: Computation efficiencies for BADI and LUSGS pretreatment.

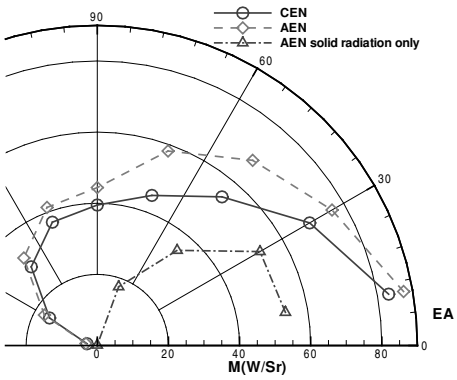

Figure 21: Distributions of the radiation intensities between 3-5 μm band.

The temperature distributions of the solid walls of the sleeve and the primary nozzle are shown in Fig. 19. The temperature of the sleeve is much higher than the total temperature of ejecting flow or ambient flow (308.5 K). This is apparently due to the radiation heat transfer of the outer wall of the primary nozzle.

The iteration convergence information in solving the solid temperature field is shown in Fig. 20. It can be seen that LUSGS pretreatment cannot guarantee computation stability.

The radiation signature of the two nozzles at different elevation angles (EA) are presented in Figs. 21-22. It can be seen that the CEN radiation signature is smaller than that of the AEN.

Fig. 23 indicates that, being different from convergent nozzles [31], the CEN's trailing edge clearly does not shorten the jet length compared to a convergent-divergent nozzle. The CO_2 mass-concentration and velocity contours of both nozzles are shown in Fig. 24. It can be seen that the thickness of the boundary layer for the CEN is much greater, implying much faster mixing, than that for the AEN. Thus, the overall temperatures of

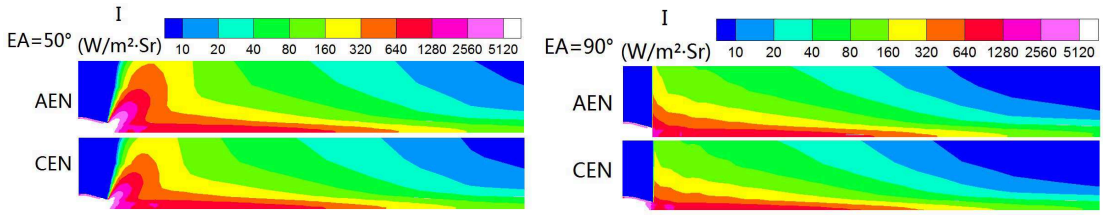

Figure 22: Contours of the radiance between 3-5 μm band at 2 elevation angles.

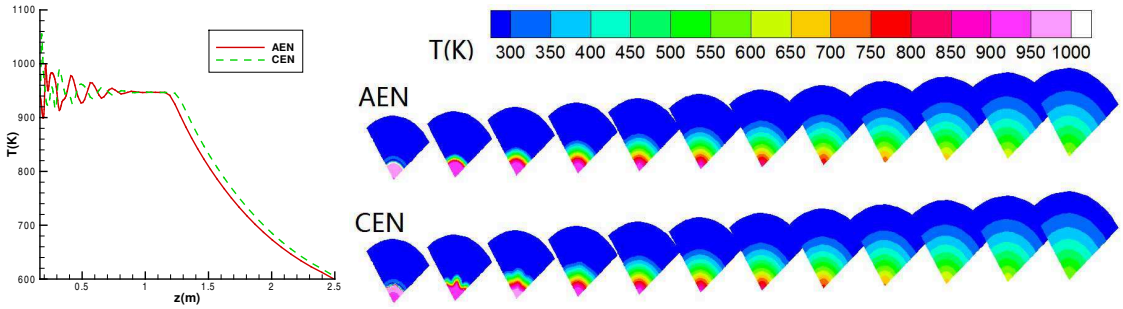

Figure 23: Comparison of AEN-CEN temperature distributions along the jet central line.

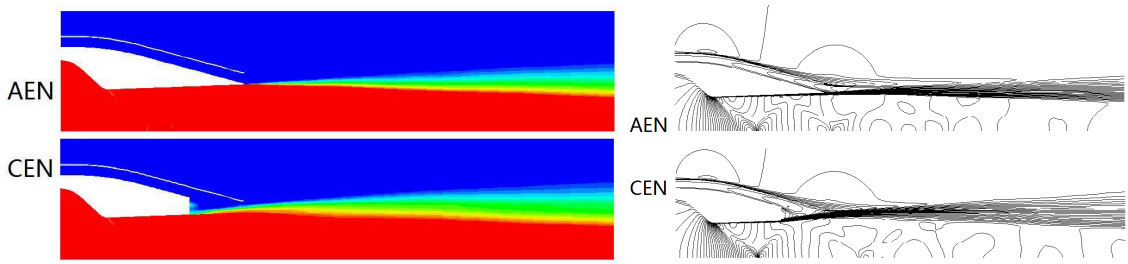

Figure 24: CO_2 mass-concentration (left) and Mach-number contours (right) of both nozzle types.

the entire hot jet are lower for CEN than for AEN. It is known that the gas radiation emission intensity is approximately proportional to the 4^{th} power of temperature (the Stefan-Boltzmann Law); hence the gas radiation signature is smaller for CEN than for AEN.

6 Conclusions

The SNBCK model has been in development for several years, but previous work had just applied the model to infrared predictions on simple-shaped structures, such as the cuboid furnace and the axisymmetric plume. Combining with the finite volume method

as treated in this paper, the SNBCK model can be applied now to the prediction of radiation heat transfers and radiation signals from complex-shaped fluid machinery (such as the axisymmetric and Chevron ejecting nozzles). Moreover, being different from previous calculation methods, which commence with calculations of the flow field and solid heat conduction (without considering radiation heat transfer) and then infrared radiation, a coupled model covering the just-mentioned physical phenomena was constructed and employed in this paper. The results show that the effects of gas radiation on the solid wall temperature cannot be neglected; moreover, the solid wall radiation, accounting for more than half of the nozzle radiation signal, is proportional to the fourth power of the solid wall temperature, and therefore it is necessary to perform a more integrated calculation with respect to radiation transfers. In this aspect, we find the following:

1. The stiffness of the two-equation turbulence model is one of the key factors affecting computational efficiency of the coupled model. The mixed analytical-numerical algorithm, which has been proposed and applied here, provides highly-improved computational efficiency by significantly reducing the stiffness.

2. By applying BADI pretreatment, the computation efficiency and stability are higher than that by LUSGS pretreatment if the BI-CGSTAB algorithm is used to deal with the ill-conditioned matrix appearing in the coupled problem between flow and solid heat conduction.

3. Treating the radiation symmetry plane as a mirror surface has been validated to be effective and accurate.

4. Chevron's trailing edge can not decrease effectively the jet length from a convergent-divergent nozzle in the under-expanded state, but can enhance the mixing effect of the main jet flow /ejecting flow /ambient flow. It also increases the thickness of the low-temperature boundary layer in aft jet flow with high radiation absorptivity, which clearly reduces the infrared radiation signature of CENs compared to AENs.

References

[1] H. Tan, X. Xia, L. Liu and L. Ruan, Numerical calculation of infrared radiative properties and transfer, Harbin: Harbin Institute of Technology Press, 2006 (in Chinese).
[2] J. Strohle and P. J. Coelho, On the application of the exponential wide band model to the calculation of radiative heat transfer in one- and two-dimensional enclosures, Int. J. Heat Mass Transfer, 45 (2002), 2129–2139.
[3] S. J. Young, Nonisothermal band model theory, Journal of Quantitative Spectroscopy & Radiation Transfer, 18 (1976), 1–28.
[4] O. Marin and R. O. Buckius, Wide band correlated-k approach to thermal radiative transport in nonhomogeneous media, J. Heat Transfer, 119 (1997), 719–729.
[5] F. Liu, G. J. Smallwood and O. L. Gulder, Application of the statistical narrow-band correlated-k method to low-resolution spectral intensity and radiative heat transfer calculation — effects of the quadrature scheme, Heat and Mass Transfer, 43 (2000), 3119–3135.

[6] J. Strohle, Assessment of the re-ordered wide band model for non-grey radiative transfer calculations in 3D enclosures, Journal of Quantitative Spectroscopy & Radiative Transfer, 109 (2008), 1622–1640.
[7] P. L. Roe, Approximate Riemann solvers, parameter vectors, and difference schemes, J. Comput. Phys., 43 (1981), 357–372.
[8] P. Gerlinger and J. Algermissen, Numerical simulation of supersonic combustion problems using an implicit LU-SGS scheme and k-epsilon or q-omega turbulence closure, AIAA-93-5021.
[9] C. G. Speziale and S. Thangam, Analysis of an RNG based turbulence model for separated flows, Int. J. Eng. Sci., 10 (1992), 1379–1388.
[10] N. Zhou and A. Krishnan, Numerical simulation of coupled heat transfer characteristics for flow at supercritical pressure, AIAA 96-178.
[11] S. T. Imlay, M. Oetrisno and D. W. Roberts, Coupled flow and heat transfer analysis using structured-unstructured grids, AIAA 96-0622.
[12] A. Soufiani and J. Taine, High temperature gas radiative property parameters of statistical narrow-band model for H_2O CO_2 and CO and correlated-k model for H_2O and CO_2, Int. J. Heat Mass Transfer, 40 (1997), 987–991.
[13] Q. Yan, Numerical Analysis, Beijing: Beijing University of Aeronautics and Astronautics Press, 2000 (in Chinese).
[14] F. Liu, G. J. Smallwood and O. L. Gulder, Application of the statistical narrow-band correlated-k method to non-grey gas radiation in CO_2-H_2O mixtures: approximate treatments of overlapping bands, Journal of Quantitative Spectroscopy & Radiative Transfer, 68 (2001), 401–417.
[15] ANSYS FLUENT 12.0 Theory Guide, 2009.
[16] Y. Zheng, Y. Shen, D. Qiu and J. Xia, Efficient elliptic solver for the mild slope equation using BI-CGSTAB method, China Ocean Engineering, 14 (2000), 175–184.
[17] R. F. Chen and Z. J. Wang, An improved LU-SGS scheme with faster convergence for unstructured grids of arbitrary topology, AIAA 99-4935.
[18] B. Merci, J. Steelant, J. Vierendeels, K. Riemslagh and E. Dick, Treatment of source terms and high aspect ratio meshes in turbulence modelling, AIAA 99-3371.
[19] A. Harten, High resolution schemes for hyperbolic systems of conservation laws, J. Comput. Phys., 49 (1983), 357–393.
[20] T. Du, Z.-N. Wu and Y. Yang, Mixed analytical/numerical method and its application to problems of turbulent flow simulation, Acta Aeronautica Et Astronautica Sinica, 27 (2006), 198–203 (in Chinese).
[21] T. Du, J. Shi and Z.-N. Wu, Mixed analytical/numerical method for flow equations with a source term, Computers & Fluids, 32 (2003), 659–690.
[22] B. Merci, J. Steelant and J. Vierendeels, Computational treatment of source terms in two-equation turbulence models, AIAA J., 38 (2000), 2085–2093.
[23] Y. Zhao, Stable computation of turbulent flows with a low-Reynolds-number k-ε turbulence model and explicit solver, Advances in Engineering Software, 28 (1997), 487–499.
[24] J. A. Meijerink and H. A. Van der Vorst, Guidelines for the usage of incomplete decompositions in solving sets of liner equations as they occur, J. Comput. Phys., 44 (1981), 134–155.
[25] P. L. T. Brian, A finite-difference method of high-order accuracy for the solution of three-dimensional transient heat conduction problems, AIChE J., 7 (1961), 367–370.
[26] J. R. Carlson, Computational prediction of isolated performance of an axisymmetric nozzle at Mach number 0.90, NASA T-M-4506, 1994.

[27] Q. Liu, P. Cinnella and L. Tang, Coupling heat transfer and fluid flow solvers for multi-disciplinary simulations, AIAA 2004-996.
[28] Chui and P. M. J. Hughes, Implementation of the finite volume method for calculation radiative transfer in pulverized fuel flame, Combustion Science and Technology, 92 (1993), 225–242.
[29] S. Dong, H. Tan, Q. Yu and L. Liu, Infrared radiative spectral band-model parameters for water vapor in the 300-3000K temperature range, Journal of Engineering for Thermal Energy and Power, 16 (2001), 33–38 (in Chinese).
[30] C. B. Ludwig, C. C. Ferriso and L. Acton, High-temperature spectral emissivities and total intensities of the 15-μ band system of CO_2, JOSA, 56 (1966), 1685–1692.
[31] H.-Y. Huang and Q. Wang, Coupled flow-heat transfer simulations of axisymmetric nozzle with chevron trailing edge, The 9^{th} Asian International Conference on Fluid Machinery, AICFM9-079, 2007.